Spatially patterned neutralizing icosahedral DNA nanocage for efficient SARS-CoV-2 blocking

Jialu Zhang[a] [b] [+], Yunyun Xu[b] [+], Miao Sun[a], Siwen Liu[c], Shuang Wan[a], Honglin Chen[c], Chaoyong Yang[a] [b], Yang Yang[b]* and Yanling Song[a]*

Abstract

New neutralizing strategies against SARS-CoV-2 and associated variants are urgently needed for the treatment of COVID-19. Targeting the SARS-CoV-2 multi-spike trimers, an icosahedral DNA framework was assembled to spatially arrange up to thirty neutralizing aptamers (IDNA-30) with nanometer precision to inhibit viral infection. Each triangular plane of IDNA-30 is composed of three precisely positioned aptamers topologically matching SARS-CoV-2 spike trimer, thus forming a multivalent spatially patterned binding. Additionally, due to its multiple binding sites and moderate size, multifaced IDNA induces aggregation of viruses. Moreover, the rigid icosahedron framework afforded by four-helixes not only forms a steric barrier to prevent the virus from binding to host, but also limits the conformational transformation of SARS-CoV-2 spike trimer. Combining multivalent topologically patterned aptamers with structurally well-defined nano-formulations, IDNA-30 exhibits excellent neutralization against SARS-CoV-2 and a broad neutralizing activity against several mutant strains. Overall, this spatially matched neutralizing strategy provides a new direction for the assembly of neutralizing reagents to enhance the inhibitory effect of SARS-CoV-2 infection and combat other disease-causing viruses.

[a] The MOE Key Laboratory of Spectrochemical Analysis & Instrumentation, the Key Laboratory of Chemical Biology of Fujian Province, State Key Laboratory of Physical Chemistry of Solid Surfaces, Department of Chemical Biology, College of Chemistry and Chemical Engineering, Xiamen University, Xiamen, Fujian 361005, China.   [b] Institute of Molecular Medicine, Renji Hospital, Shanghai Jiao Tong University School of Medicine, Shanghai Jiao Tong University, Shanghai, 200127, China.   [c] State Key Laboratory for Emerging Infectious Diseases and InnoHK Centre for Infectious Diseases, Department of Microbiology, Li Ka Shing Faculty of Medicine, the University of Hong Kong, Hong Kong SAR, China.

[+] These authors contributed equally to this work: Jialu Zhang, Yunyun Xu

Corresponding author E-mail: yang.yang.nano@sjtu.edu.cn; ylsong@xmu.edu.cn

To date, SARS-CoV-2 virus has caused a global pandemic and the constantly emerging new variants have posed challenges to prophylaxis and postexposure therapy. The SARS-CoV-2 virus hijacks the angiotensin-converting enzyme-2 (ACE2) of host cells by the spike trimer (S trimer) on the viral surface[1]. One promising approach to inhibit viral infection is development of neutralizing reagents which block the interaction of S trimer-ACE2 with high efficacy, resulting in efficient inhibition of the SARS-CoV-2 invasion pathway. Most viruses engage with host cells by multivalent interactions, enabling efficient cell attachment and realization of the infection process. Furthermore, the spikes of most enveloped viruses are distributed at distinctive distances with specific geometric patterns, resulting in unique infection features[2, 3]. The enormous enhancement of the natural interaction between receptors and ligands can be easily accomplished due to the more orderly and topological arrangements of multivalent ligands[4]. Therefore, topologically ordered multivalent neutralizing reagents have high potential to improve the neutralization efficiency and resist mutational escape, compared to monovalent neutralization reagents.

However, introduction of neutralizing antibodies in certain multivalent nanodevices causes cumbersome and time-consuming conjugate workflow[5]. Compared with the complicated customization modification of neutralizing antibodies, neutralizing aptamers, which are essentially nucleic acids, can be programmed and assembled onto various nanodevices for scalable applications[6]. Moreover, aptamers exhibit the distinctive advantages of low cost, low immunogenicity, and facile, controllable production with little batch-to-batch variation. Recently we and other groups have identified several neutralizing agents against SARS-CoV-2, in the form of monovalent[7-12], bivalent aptamers[13] as well as spherical aptamers[14] based on gold nanoparticles, the ability of topological control has rarely been realized, exhibiting unsatisfactory therapeutic efficacy or leading to the introduction of unnatural nano-scaffolds. Therefore, it is of utmost importance to develop a spatially matched neutralizing aptamer

69   based-strategy against SARS-CoV-2 and its unknown mutants.

70   The programmability of DNA nanostructures offers delicate tools to

71   precisely regulate other molecules in terms of number, location and relative

72   distance over space[15-17]. Furthermore, spatially arranged molecules may

73   work collectively or associatively to achieve better efficiency compared to

74   a disordered array[18]. Therefore, a DNA nanodevice equipped with

75   neutralizing aptamers in a precise pattern may be promising for realization

76   of a SARS-CoV-2 blockade. Considering the features of the SARS-CoV-2

77   S trimer and its infection mechanism [19], we employed an icosahedral DNA

78   origami framework to present SARS-CoV-2 neutralizing aptamers with

79   specifically assigned numbers and spatial locations to block the interaction

80   between the S trimer and host ACE2 (**Fig. 1a**).
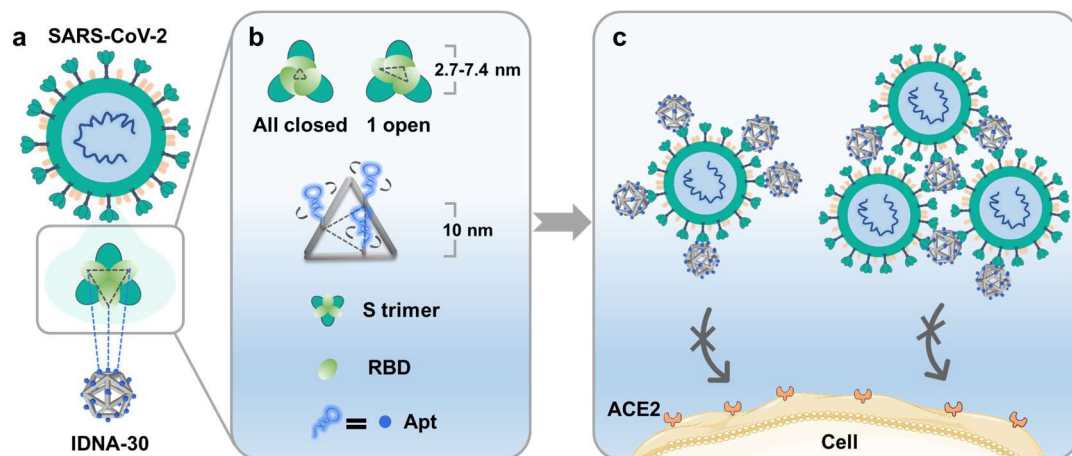
81 **Figure 1. Spatially matched multisite locking strategy of IDNA-30 against SARS-**
82 **CoV-2.** The distances between different monomers of S trimer change with the open
83 state of the receptor binding domain (RBD). Even though the spacing of aptamers on
84 the same plane is ca.10 nm, the extended area of the aptamer fluctuates by ca.10 nm.
85 Additionally, there may be several possible binding modes when adjacent subunits or
86 adjacent proteins combine with aptamers.

87

Results

89   **Design and characterization of neutralizing icosahedral DNA**
90 **nanocage.** Considering the triangular pattern of the S trimer, as a regular
91 polyhedron with the most equilateral triangular faces, an icosahedral DNA
92 origami was prototyped to carry n neutralizing aptamers (termed IDNA-n,
93 n≤30). First, IDNA-n can serve as an isotropic nanoparticle with 20

equilateral triangular faces holding 0~3 blocking agents on each face (ca.10 nm) against the S trimer (~13 nm in diameter[20]). In addition, by virtue of the relatively excellent molecular flexibility of toehold sequence (~7 nm), IDNA-n provides an accessible molecular handle to trap receptor binding domains (RBDs) (**Fig. 1b**), circumventing the size fluctuations resulted from conformational transitions of RBDs in the S trimer[21] (2.7~7.4 nm, **Supplementary Fig. 1**). For complete decoration, through complementary strand hybridization, each triangular plane of IDNA-30 equips three precisely located aptamers topologically matched with the spike trimer of SARS-CoV-2. As a result, combining the topologically matched aptamer trimers and flexible DNA connectors, IDNA-30 can boost binding affinity and neutralization efficacy, avoiding the potential dissociation of single-point inhibition. Second, multifaced IDNA-30 could potentially induce aggregation of viruses due to multivalent binding and its moderate size, which can slow the movement of viruses and thus further reduce SARS-CoV-2 infection (**Fig. 1c**). Third, the rigid framework afforded by four-helixes on each side not only provides a steric barrier for S trimer-ACE2 interaction, but also limits S trimer conformational transformation, thus further inhibiting viral membrane fusion. More importantly, the neutralizing aptamers display relatively compact arrangement and prevent accessibility by nuclease, reducing the degradation of DNA. Therefore, combining multivalent topologically patterned aptamers with structurally well-defined nano-formulations, IDNA-30 is capable of inhibiting SARS-CoV-2 infection at multiple levels, enhancing the therapeutic efficacy.

As shown in **Fig. 2a** and **Supplementary Fig. 2**, the icosahedral DNA framework (possessing 12 vertices, 30 edges and 20 faces) was designed via the software Tiamat and constructed by a 7560nt scaffold and 216 staples. Different from the reported icosahedral DNA origami with double-helix edges, our edges were intentionally designed as four-helix bundles (63nt, ~21 nm in length; 5 nm in thickness) to achieve enhanced structural rigidity and stability. Considering this DNA icosahedron as a bilayer of double-helix framework, staples at the vertices were tailored to generate unbalanced tensions at the outer and inner layer and assure the unique wrapping topology, therefore, aptamers were guaranteed to present at only

128 the outer surface. Compared with disordered and uncertain multivalent
129 recognition, this distinctive structure provided more unequivocal areas for
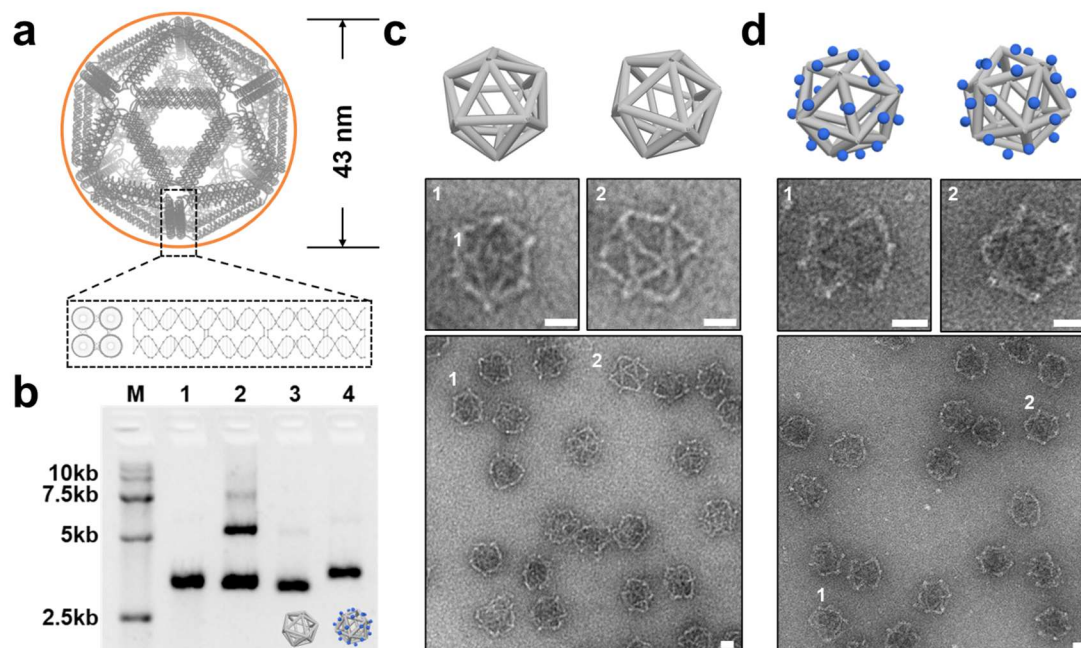
130 receptor-ligand recognition, achieving more efficient binding.

Figure 2. Design and characterization of ID and IDNA-30. a, 3D cartoon model of
ID. ID has rigid frame configuration owing to the bundle of 4 helixes bundle on each
side. **b,** 1.5 % Agarose gel electrophoresis analysis of DNA nanostructures (lane 1:
scaffold 7560, lane 2: unpurified ID, lane 3: ID, lane 4: IDNA-30). The TEM images
of **c,** ID and **d,** IDNA-30. IDNA-30 was obtained by orderly arrangement of aptamers
on ID. Scale bar =20 nm.

138 By virtue of the high programmability of DNA nanostructures,
139 neutralizing aptamers with elongated anti-toehold sequences could be
140 immobilized at the assigned toehold sites on the edges to achieve a
141 controllable pattern. In the case of a fully decorated frame IDNA-30, the
142 flexibility provided by the 21bp (~7 nm) toehold pairs allowed the
143 neutralizing aptamers to wander and offer relatively dynamic locking
144 patterns against the S trimers. Since the theoretical distance between
145 adjacent S1 subunits of the S trimer changes by 2.7~7.4 nm with the
146 conformational transition of RBD[21], three coplanar aptamers were able to
147 provide more compact binding sites to attack one S trimer. Meanwhile, the
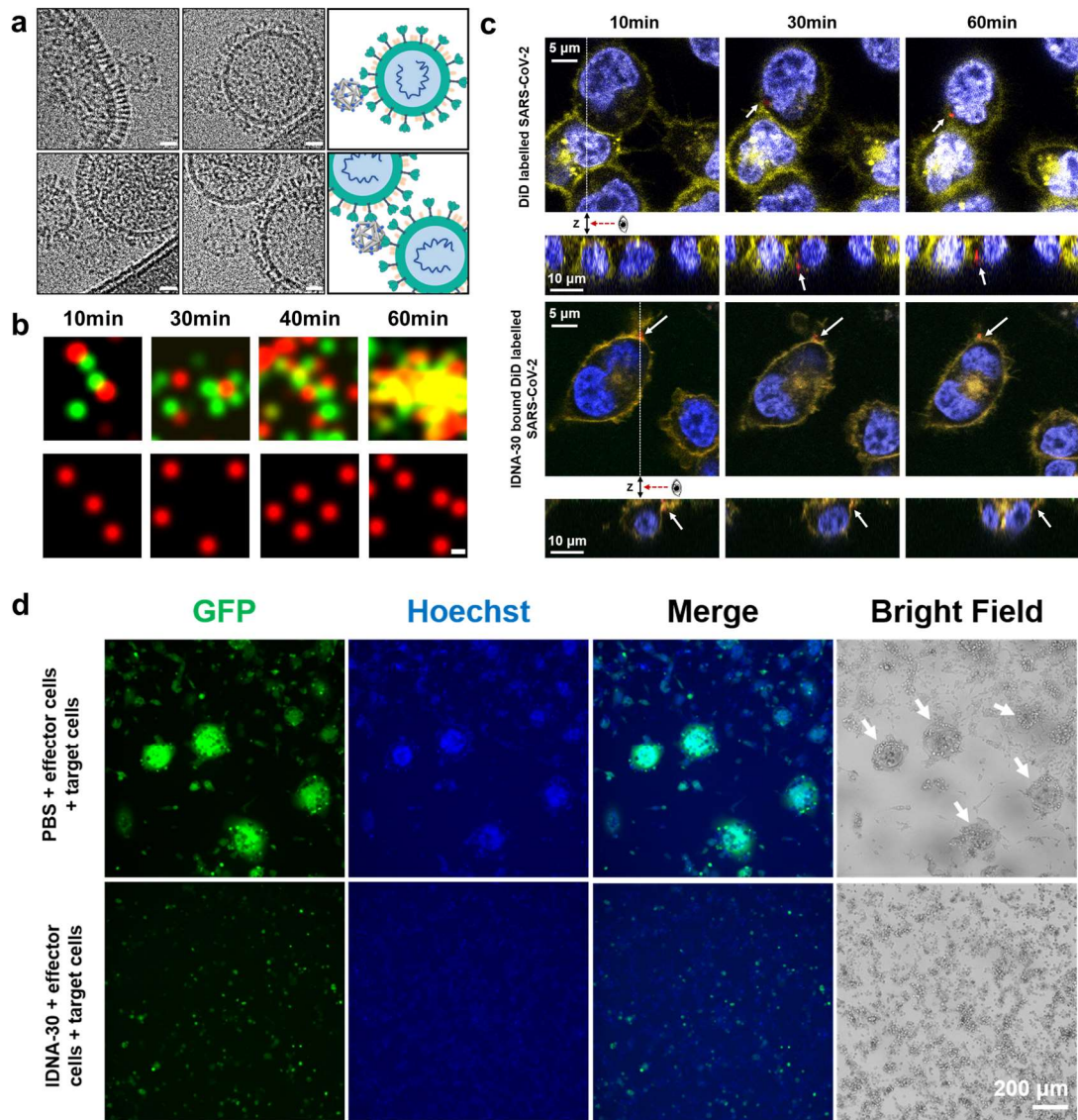148 peripheral neutralizing aptamers were still available to grab surrounding S

trimers to enhance the binding, while the remote neutralizing aptamers were also free to bind and lock onto another virus particle (**Fig. 1**).

First, ID was acquired by thermal annealing of numerous single-stranded DNA (**Supplementary Table 1-3**) and purified by rate-zonal centrifugation. Compared with ID, the decreased mobility of IDNA-30 in agarose gel electrophoresis (AGE) indicated successful assembly of neutralizing aptamers (**Fig. 2b**). Transmission electron microscopy (TEM) imaging further demonstrated the topology and size of the well-composed ID, which were in accordance with the theoretical design (**Fig. 2c**). IDNA-30 maintained the same formation and dispersion (**Fig. 2d**), even after storage at 4℃ for 7 days (**Supplementary Fig. 3**). Moreover, IDNA-30 showed outstanding structural integrity after even 35 days of storage at 4℃ (**Supplementary Fig. 4**). To evaluate the stability of IDNA-30 against nuclease degradation in a biological matrix, IDNA-30 was incubated with DMEM cell media with 10 % fetal bovine serum at 37℃ for several hours. The bands from the AGE image showed that the IDNA-30 remained sufficiently stable even after 48 h incubation. This stability is likely due to the dense spatial arrangement of aptamers in IDNA-30, as well as the inherent electronegativity and nick-hidden strands of ID (**Supplementary Fig. 5**). Such excellent stability of IDNA-30 indicates its promise as a foundation for subsequent applications in complex biological systems.

Study of the binding mode of SARS-CoV-2 pseudovirus with IDNA-30. Next, we investigated the interaction between virions and IDNA-30 by imaging experiments. Cryo-EM images showed S trimers with nail-like shape embedded in the envelope of SARS-CoV-2 pseudovirus, consistent with a previous study of authentic SARS-CoV-2[22] (**Fig. 3a**, **Supplementary Fig. 6**). Each IDNA-30 binds to more than one spike trimer in a single virus (**Fig. 3a, up**), and also can serve as a connector to form a poly-viral complex (**Fig. 3a, bottom**), suggesting the role of multivalent receptor-ligand interaction. In detail, the aptamers of IDNA-30

Figure 3. Characterization of the binding mode of SARS-CoV-2 pseudovirus with IDNA-30. **a,** Cryo-electron microscopy (cryo-EM) of SARS-CoV-2 pseudovirus bound with IDNA-30. Scale bar=20 nm. **b,** Different time points of selected confocal frames from top row: virus particles (red) incubated with IDNA-30 (green) and bottom row: virus particles (red) at room temperature. Scale bar = 1 μm. **c,** Confocal imaging. Top row: viral accumulation over time for the no-inhibitor treated condition. Bottom row: viral entry inhibition over time during IDNA-30 treatment. An eye symbol of cross-sections at each time point represents the observation direction (along the dotted lines in the above images). The cross-sections reconstructed from Z stacks, with twenty images taken at different focal planes (spacing: 1 μm). Cell nuclei (blue), cell membrane (yellow) and virus (red) were stained with Hoechst, Dil and DiD, respectively. The white arrows point to representative viral particles. **d,** Representative images of 293T-SARS-CoV-2-Spike-Del18-HA-OE(GFP) cells pretreated without or

193 with 15 nM IDNA-30 before co-culturing with ACE2-transfected HEK293T cells for

194 48 hours are displayed. The white arrows point to representative syncytium formation.

195 293T-SARS-CoV-2-Spike-Del18-HA-OE-GFP and ACE2-transfected HEK283T cells

196 were defined as effector cells and target cells, respectively.

197 are bound with the S trimers and provide steric hindrance against receptor

198 binding (**Supplementary Fig. 7**). Therefore, this face-to-face blocking

199 strategy not only achieves spatial multisite synergy, but also has potential

200 to deal with antigenic drift through spatial multisite locking to interrupt

201 subsequent viral invasion.

202 Two primary binding modes can be speculated based on different ratios

203 of particle concentration of virions incubated with IDNA-30

204 (**Supplementary Fig. 8**). On one hand, even though S trimers are

205 distributed randomly and sparsely on the surface of SARS-CoV-2[22], in the

206 case of (locally) low IDNA-30 to virion ratio, IDNA-30 can serve as a

207 connector, resulting in aggregation of virions, which can slow the mobility

208 rate of SARS-CoV-2. On the other hand, at (locally) high IDNA-30 to

209 virion ratio, some virions are covered with IDNA-30, termed

210 "dreamcatcher", which reduces the accessibility to host receptors. Confocal

211 images of unbound or IDNA-30-bound virions with the same order of

212 magnitude particle concentration were consistent with the results of cryo-

213 EM and TEM (**Fig. 3b**, **Supplementary Fig. 8**). The aggregation

214 phenomenon emerged gradually after virions were incubated with particle

215 concentration of 2.5 times IDNA-30 at room temperature for 30 min (**Fig.**

216 **3b**, **Supplementary Fig. 9**). Remarkably, IDNA-30-bound virions exhibit

217 marked size expansion compared to free virions. Due to the increase of

218 mass, the larger nanoparticles display a lower range of movement with

219 slow mobility based on the Brownian motion principle.

220 To further explore the SARS-CoV-2 infection, we tracked entry of DiD-

221 labeled SARS-CoV-2 pseudovirus into the host cells by time-lapsed

222 confocal imaging. Compared to unbound virions, IDNA-30-bound virions

223 flowed on the cell membrane, reducing the binding of virions and cells,

224 and even decreasing the opportunity of entering cells over time (**Fig. 3c**,

225 **Supplementary Fig. 10**). Two main reasons are speculated to explain this

226 phenomenon. On one hand, larger complexes block the mobility of IDNA-

30-bound virions when they were introduced to cells. On the other hand, considering negative charges from both DNA backbone and virion surface proteins, viral entry inhibition may be ascribed to the enhanced electrostatic repulsion between the host cell and IDNA-30-bound virions. Additionally, there was no obvious cell internalization even after incubation of IDNA-30 with cells at 37 °C for 4 h (**Supplementary Fig. 11**). Quantitative assay by flow cytometry corroborated these results (**Supplementary Fig. 12**).

Moreover, we speculated another underlying mechanism that IDNA-30 could interrupt the membrane fusion of viruses and host cells. As the energy driven post-fusion conformation is irreversible, the infection process would be blocked for premature activation of S trimer's conformational changes for fusion[23]. Therefore, we constructed HEK 293T cells expressing SARS-CoV-2 Spike-Del18 protein and ZsGreen on the cell membrane (effector cells) to obtain a macroscopic perspective of the receptor-ligand mediated cell-cell fusion. After mixing the effector cells and ACE2-expressing HEK293T cells (target cells) at an equivalent ratio, SARS-CoV-2 S trimers could trigger ACE2-related membrane fusion without inhibition of IDNA-30, consistent with the plasma membrane fusion pathway of SARS-CoV-2 reported previously[23] (**Fig. 3d**, **Supplementary Fig. 13**). The syncytium formation and weaker fluorescence intensity of fused cells indicated the successful establishment of infection. However, in the presence of IDNA-30, the decreased syncytium revealed that cell-cell fusion tendency was significantly weakened. In light of above-mentioned underlying mechanism, IDNA-30 holds promise as an alternate choice of SARS-COV-2 neutralizing reagent, rather than neutralization by the aptamer itself.

In vitro SARS-CoV-2 pseudovirus inhibition. Next, to demonstrate the inhibition of pseudovirus infection by IDNA-30, we carried out a neutralization assay as displayed in **Supplementary Fig. 14**. Owing to the multivalent collaboration and steric barrier caused by IDNA-30, the neutralizing efficiency of IDNA-30 (82.8%) was ~7 times higher than the monomer aptamer's efficiency (12.1%) (**Figs. 4a, b**). At the same

concentration, a commercial neutralizing antibody (Research Resource Identifiers Number: AB_2857935) showed inferior neutralization (68.0%) (**Fig. 4b**). Remarkably, instead of the infectious cell count the images in **Fig. 4a**, measurement based on the overall fluorescence intensity, neutralized pseudovirus SARS-CoV-2 exhibited a half-maximal inhibitory concentration (IC_{50}) was 0.82 aM, corresponding to an inhibitory ability of 91.7 % (**Fig. 4c**), indicating superior neutralization compared to previous aptamer-based neutralization (**Supplementary Table 5**).
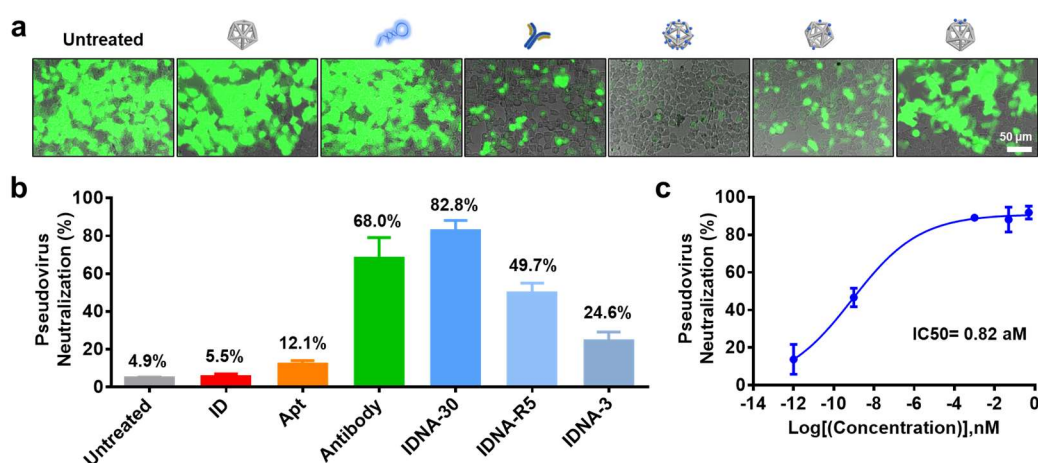
Figure 4. Assessment of pseudotyped SARS-CoV-2 neutralization assay. a, Fluorescence images and **b,** bar graph of infection efficiency for SARS-CoV-2 pseudovirus treated with 1 nM ID, Apt, Antibody, IDNA-30, IDNA-R5 and IDNA-3. IDNA-3 and IDNA-30 were engineered with a deterministic arrangement, while IDNA-R5 was functionalized with aptamers randomly. **c,** Pseudovirus neutralization curve of IDNA-30.

To further demonstrate the advantages of IDNA-30, we designed two control groups that IDNA-3 (three aptamers with coplanar precise distribution pattern, **Supplementary Fig. 2**, **Supplementary Table 1, 2, 4**) and IDNA-R5 (five aptamers with random distribution pattern, **Supplementary Fig. 2**). Neutralization by IDNA-30 exhibited much higher potency than that of IDNA-3 (24.6 %) (**Fig. 4b**), suggesting that the arrangement of multivalent aptamers of IDNA-30 provides effective inhibition of viral infection. The neutralizing ability of IDNA-R5 (49.7 %)

displayed twice that of IDNA-3, mainly due to the random biodistribution of S trimers and steric hindrance of the scaffold. Furthermore, the random distribution of aptamers in IDNA-R5 indicated the scalability and high utilization rate of small amounts of ligands. Collectively, by exploiting the spatial multisite locking and rigid framework blocking, IDNA-30 is an alternative neutralizing nano-reagent for SARS-CoV-2.
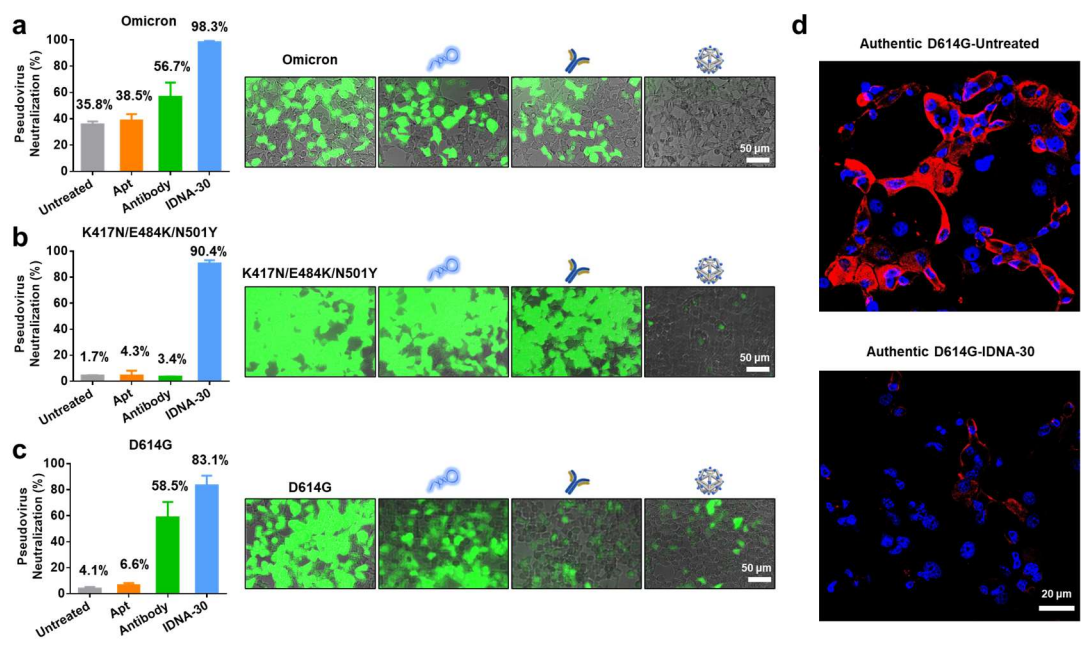
***In vitro* mutant pseudotyped and authentic SARS-CoV-2 inhibition.**
The evolution of SARS-CoV-2 is raising broad concern, not only due to enhanced infectiousness, but also because the unlimited mutations could weaken the effectiveness of certain neutralization antibodies or vaccines[24]. New variants tend to display the accumulation of multiple mutations to cope with a changeable environment. Remarkably, IDNA-30 displayed delightful neutralization against Omicron pseudovirus with over 98.0% neutralization efficiency (**Fig. 5a**), having the potential to overcome the dilemma that Omicron escapes majority of existing SARS-CoV-2 neutralizing antibodies[24]. Subsequently, we further probed the cases of single mutant (D614G) and triple mutant (K417N/E484K/N501Y), which have played pivotal roles in the viral invasion of SARS-CoV-2 variants[25]. As expected, the inhibition ability of a monomer aptamer was negligible in both cases, verifying the limitations of single point blocking encountered off-target. Moreover, the antibody exhibited relatively reduced efficiency of neutralization against a single mutant (**Figs. 4b and 5c**), and complete loss of neutralizing effect against multiple mutant (Omicron) (**Fig. 5a**) and a triple mutant (**Fig. 5b**). This may be attributed to antigen drift. In contrast, IDNA-30 still demonstrated high potency against a single mutant with 83.1 % and a triple mutant with 90.4 % neutralization efficiency (**Figs. 5b, c**).

With collaborative recognition by multivalent aptamers, larger IDNA-30-bound virus complexes showed hindered invasion speed. Simultaneously, the steric barriers caused by IDNA-30 blocked subsequent viral membrane fusion. It is also striking that 10 pM IDNA-30 displayed potent neutralization potency (85.5 %) against the authentic virions with

D614G mutation (GenBank: MT835143.1) (**Fig. 5d**). Additionally, compared with the untreated group, the fluorescence intensity of infectious cells of IDNA-30 was relatively dim, suggesting that fusion of virus and host membrane was prevented by IDNA-30. Cumulative evidence shows that IDNA-30 exhibits excellent and robust neutralization and has outstanding potentials in developing novel prophylaxis and therapeutics strategies to confront the COVID-19 pandemic.

Figure 5. Assessment of mutant pseudotyped and authentic SARS-CoV-2 neutralization assay. a, Fluorescence bar graphs and neutralization potency of pseudovirus SARS-CoV-2 (Omicron) that treated 15 nM Apt, Antibody and IDNA-30. **b,** Fluorescence bar graphs and neutralization potency of pseudovirus SARS-CoV-2 with K417N/E484K/N501Y mutations treated with 10 nM Apt, Antibody and IDNA-30.**c,** Fluorescence images and neutralization potency of 5 nM Apt, Antibody and IDNA-30 that target the pseudovirus SARS-CoV-2 with D614G mutation. **d,** Images of IDNA-30 neutralization of authentic SARS-CoV-2 with D614G variant infection of Vero E6 cells. Up: Untreated; Bottom: 10 pM IDNA-30. The fixed cells were stained by Hoechst dye (blue) for the cell nucleus and an anti-SARS-CoV-2 nucleocapsid antibody (red) for the virus.

Finally, the safety of IDNA-30 was tested. Although any foreign molecule may cause potential immunogenicity, DNA nanostructures, in general, exhibit minimal-toxicity, superior biocompatibility and low immunogenicity[26, 27]. As expected, the cytotoxicity of IDNA-30 was

undetectable, even at a concentration of 10 nM (**Supplementary Fig. 15**). Moreover, there was no white blood cell response to IDNA-30 (**Supplementary Fig. 16**), negligible change in the cytokine level of mouse plasma (**Supplementary Fig. 17**), and normal histological results (**Supplementary Fig. 18**), demonstrating that IDNA-30 is immunologically inert, which is conducive to the development of subsequent practical applications.

Conclusions

In summary, we designed an icosahedral DNA framework as a rigid scaffold that is functionalized by neutralizing aptamers in a controllable fashion to achieve spatially multisite binding for inhibition of SARS-CoV-2 infection. Although many kinds of icosahedra have been developed previously[15, 28], an icosahedron with four helixes per side showed much higher structural homogeneity, which provides ligands with more unequivocal spatial pattern recognition domains. Benefiting from the rigid framework and high programmability, IDNA-30 displayed excellent inhibitory ability by disrupting the virus and hijacking the host cellular receptor. Compared with a disorderly group collaboration of aptamers, multiple aptamers of the IDNA-30 are expected to achieve more efficient neutralization in a controlled arrangement. The spatial multisite locking and steric hindrance by IDNA-30 facilitated the inhibition of aptamers against the virus. The confined conformational shift of S trimers shown by cell-cell fusion indicates the broader neutralization by IDNA-30. Furthermore, the clusters formed by IDNA-30-bound viruses displayed slow mobility during the infection process, possibly providing a responsive window period for immune cells. This programmable aptamer-integrated DNA nanostructure provides an excellent choice for the prophylaxis and postexposure therapy of SARS-CoV-2 or other viruses and pathogens with defined antigen structures. Given the distinctive structures and infectious mechanisms of various viruses, we expect that more matched aptamers and customized DNA nanostructures will be integrated to combat other viruses in the future.

374

Methods

Materials and reagents. DNA sequences were synthesized and purified using HPLC by Generay Biotech Co., Ltd, Shanghai, China and Sangon Biotechnology, Shanghai, China. Dulbecco's modified Eagle's medium (DMEM, Gibco), penicillin–streptomycin (Gibco), trypsin-EDTA (Gibco), fetal bovine serum (FBS, Gibco) and red blood cell lysis materials (Cat. 00-4300-54) were purchased from Thermo Fisher Scientific. Hoechst 33342, Enhanced cell counting kit-8, DiD (1,1′-dioctadecyl-3,3,3′,3′-tetramethylindodicarbocyanine and 4-chlorobenzenesulfonate salt) and DiI (1,1'-dioctadecyl-3,3,3',3'-tetramethylindocarbocyanine perchlorate) were obtained from Beyotime Institute of Biotechnology, Shanghai, China. ACE2-transfected HEK293T cells, 293T-SARS-COV-2-Spike-Del18-HA-OE-GFP cells, pseudovirus-SARS-CoV-2 (catalog No. FNV215), pseudovirus-SARS-CoV-2 (D614G) (catalog No. FNV2776), pseudovirus-SARS-CoV-2 (K417N/E484K/N501Y) (catalog No. FNV3327) and pseudovirus-SARS-CoV-2 (Omicron) (catalog No. FNV4122) were purchased from Fubio Biological Technology Co. Ltd., Shanghai, China. SARS-CoV-2 Spike Neutralizing Antibody, Mouse Mab (Catalog#40592-MM57) was purchased from Sino Biological Inc (China). Uranyl formate and all chemicals for making 1x TE-Mg^{2+} buffer (50 mM Tris-HCl, 1 mM Na$_2$H$_2$EDTA,10 mM MgCl$_2$, pH = 8.0) were obtained from Sigma-Aldrich. Micro blood collection tubes (1 mL, GC007, EDTA·K2) were purchased from Jianfu Medical (Guangzhou, China). Other common chemical reagents were purchased from Sangon Biotechnology Inc., Shanghai, China.

DNA sequence design. DNA sequences were designed by Tiamat software of two- and three-dimensional DNA nanostructures, which are shown at **Supplementary Table 1**. DNA scaffold strands of 7560 bases (type p7560, Cat#1081310) derived from the genome of bacteriophage M13 were synthesized by Integrated DNA Technologies. The outer-handle sequences

(18 nt) were complementary to the aptamer toehold and manually added to the 3′-ends of the appropriate staple strands.

Preparation and characterization of the ID and IDNA. As shown in **Supplementary Table 1**, a one-pot reaction was carried out to make each DNA complex by mixing all component strands in the correct relative concentrations in 1x TE-Mg^{2+} buffer in an Eppendorf 0.2 mL PCR Tube (Corning, USA). Buffer was made from 20x TE and 100 mM MgCl$_2$ stock solution. All purified oligonucleotides were dissolved in ultrapure water. The final concentration of each DNA nanostructure was set at 20 nM. The mixture was annealed by incubating at 75 °C for 5 min followed by cooling from 65 °C to 4 °C at the rate of 1 °C every 36 min using a thermal cycler.

DNA origami was purified using density gradient centrifugation with 45 % (v/v) and 15 % (v/v) glycerin as described previously[29], and characterized by 1.5 % agarose gel electrophoresis in 0.5x TBE (10 mM MgCl$_2$) at a constant voltage of 70 V for 2.5 h. The recovered product (ID, ID-3toe or ID-30toe) was concentrated by Amicon Ultra-0.5 mL 100 kD centrifugal filters (Millipore Corporation, Bedford, USA). The concentration of ID, ID-3toe or ID-30toe were quantified using NanoDrop^{TM} one (Thermo Fisher Scientific, USA) and stored at 4 °C for subsequent use. To obtain DNA nanostructures related to the experiment, ID-3toe or ID-30toe were incubated with the corresponding ratio of aptamer in a final concentration 1x TE-Mg^{2+} buffer at 37 °C for 1 h and characterized (**Supplementary Fig. 1, Supplementary Tables 2 and 3**). The molecular weights of DNA nanostructures were summed by Integrated DNA Technologies and displayed in **Supplementary Table 4**.

Stability analysis of DNA nanostructures. DNA nanostructures (5 nM) were mixed with 80 % (volume fraction) DMEM (10 % FBS) and incubated at 37 °C for 0, 2, 4, 8, 24, 48 h. The control group was equal proportion ID and IDNA-30 separately mixed with PBS. Aliquot IDNA-30 was stored at 4 °C for 7, 14, 21, 28, 35 days before characterizing. Finally,

438   the mixtures were characterized by 1.5 % agarose gel electrophoresis in

439   0.5x TBE (10 mM $MgCl_2$) at 70 V/2.5 h.

440

441   **Transmission electron microscopy (TEM) imaging.** The particle

442   concentration of 20 nM IDNA-30 was ~10^9 particles/mL by Nanoparticle

443   Tracking Analysis (Malvern & Nanosight NS300, data not shown). The

444   particle concentration of SARS-CoV-2 pseudovirus in the samples was

445   approximately 10^{10} particles/mL (Ratios of SARS-CoV-2 pseudovirus:

446   IDNA-30 = 100:1, 80:1, 50:1, 20:1, 10:1). SARS-CoV-2 pseudovirus co-

447   incubated with IDNA-30 at 37 °C for 1 h before TEM imaging.

448   Next, all procedures were performed as follows: copper grids (400

449   square mesh, Cat# T11023, Tianld, Beijing, China) were treated by Glow

450   Discharge (PELCO easiGlowTM, Ted Pella, Inc.) at 25 mA for 60 s.

451   Subsequently, 5 μL samples were floated to the glow-discharged copper

452   grids for 1 min, blotted with ashless filter paper, washed once and stained

453   by 2 % uranyl formate with 25 mM NaOH for 1 min, and blotted dry.

454   Negative-stained TEM images were obtained using a Hitachi Transmission

455   Electron Microscope set to 100.0 kV potential. The TEM imaging of ID

456   and IDNA-30 followed above procedure at the concentration of 5 nM.

457

458   **Cryo-electron microscopy (Cryo-EM) analysis.** IDA-30 (30 nM) was

459   incubated with pseudovirus stock solution at 37 °C for 1 h, and diluted

460   twice with ultrapure water for subsequent analysis. Three μL of the fresh

461   samples was added to the glow-discharged copper grid (Lot # 111219, Cat#

462   01895-F, Lacey carbon, 300 mesh, copper, Ted Pella, Inc., USA) for 30 s

463   and blotted with ashless filter paper. Subsequently, 2.5 μL of the freshly

464   prepared sample was applied onto the glow-discharged copper grid, blotted

465   for 5 s (Blot force: 3, Wait time: 3 s; Blot Total: 1, Drain time: 0 s,

466   temperature: 22°C, humidity: 100 %) and rapidly frozen in liquid ethane

467   using a Vitrobot Mark IV (ThermoFisher Scientific, USA). All grids stored

468   in liquid nitrogen before being screened on a cryo-electron microscope

469   (Talos F200C G2, Thermo Fisher Scientific, USA) equipped with 4k × 4k

470 Ceta CCD (charge-coupled device) camera. The samples were imaged at
471 200 kV with an absolute magnification of 45000× corresponding to a pixel
472 size of 452 pm.

473

474 **Preparation of DiD-labeled SARS-CoV-2 pseudovirus particles.**
475 SARS-CoV-2 pseudovirus particles were labeled with the lipophilic
476 fluorescent dye DiD. According to previously works reported[30],
477 approximately $2×10^8$ particles were mixed with 1 nmol of DiD dissolved
478 in 3% dimethyl sulfoxide. The excess dye was removed by illustraTM
479 NAPTM-5 Columns (Cot.17-0853-01, GE Heathcare, Sweden） in HNE
480 buffer (5 mM HEPES, 150 mM NaCl, 0.1 mM EDTA, pH 7.4). About 1
481 mL DiD-labeled virus was recovered from 1 μL stock solution of virus,
482 then stored at 4 °C.

483

484 **Confocal imaging.** Images of fluorescent samples were acquired with a
485 Leica TCS SP8 confocal microscope equipped with a 63× oil-immersion
486 objective. All images were analyzed by ACE2-transfected HEK293T cells
487 inoculated on a 20 mm glass-bottom cell culture dish (NEST, China) for at
488 least 24 h at 37 °C in 5% CO_2.

489 At room temperature, 2 nM Alexa Flour-488 labeled IDNA-30
490 ($1.5×10^8$particles/mL) was added to DiD-dyed virus (~$6×10^7$ particles/mL)
491 for particle dynamic tracking at 0, 30, 40 and 60 min. The control group
492 contained only DiD-dyed virus. For time-lapsed confocal imaging, the
493 cells were labeled with both 2 μM Hoechst 33342 and 5μM Dil solution
494 for nucleus and membrane staining, respectively. Cells were washed twice
495 with PBS. After adding DiD-labeled virus (or IDNA-30-bound virus
496 stained with DiD) to the ACE2-transfected HEK293T cells stained with
497 both Dil and Hoechst 33342, imaging was conducted using confocal
498 microscopy and four fluorescence emission wavelengths, 405 nm (nucleus,
499 blue), 488 nm (IDNA-30, green), 561 nm (cell membrane, yellow), and
500 640 nm (virus, red), were detected simultaneously.

501 For cell internalization confocal imaging, 2 nM IDA-30 or 60 nM Apt

was incubated with ACE2-transfected HEK293T at 37 °C for 4 h. Cells were dyed with both 2μM Hoechst 33342 and 5μM Dil solution for membrane and nucleus staining, respectively. Then the images were obtained by using confocal microscopy at 405 nm (nucleus, blue), 488 nm (IDNA-30, green), 561 nm (cell membrane, yellow) and bright field.

Cell-cell fusion assay. Cell-cell fusion assays were evaluated by a method reported previously[23]. First, we obtained HEK293T cell lines transfected with the plasmid pAVV-IRES-SARS-CoV-2 spike Δ18 encoding the ZsGreen (293T-SARS-COV-2-Spike-Del18-HA-OE-GFP). All cells were cultured in DMEM containing 10 % FBS and 1 % penicillin–streptomycin at 37 °C in 5 % CO_2. 293T-SARS-COV-2-Spike-Del18-HA-OE-GFP and ACE2-transfected HEK283T cells were defined as effector cells and target cells, respectively.

Equal proportions of effector cells and target cells were seeded in a 96-well microplate with a total density of 10^5 cells at 37 °C for 48 h, in the absence of IDNA-30 and in the presence of 5, 10 and 15 nM IDNA-30. Next, fields were randomly chosen in each well and the cells fused or unfused with target cells were analyzed under a fluorescence microscope (Nikon Ti2-U). The fused cells were at least twice the size of the unfused cells and the fluorescence intensity in the fused cells was weaker because of the diffusion of ZsGreen from one cell to the other cell.

***In vitro* inhibition of pseudotyped SARS-CoV-2 neutralization.** Various concentrations of neutralizing agents (ID, IDNA-3, IDNA-R5, IDNA-30, Apt or Antibody) in DMEM supplemented with 10 % fetal bovine serum were incubated with pseudoviruses at 37 °C for 1 h, respectively. Then the mixtures above were added to ACE2-transfected HEK293T cells (1.6×10^4 per well in 384-well plates for culturing at least 20 h at 37 °C in 5 % CO2), respectively. After infection for 8 hours, medium was refreshed and then the cells were incubated for an additional 48 h. For fluorescence image analysis, infected ACE2-transfected HEK293T cells were displayed with

the GFP expression. The luciferase activity was calculated for the detection of relative light units using a microplate spectrophotometer (BioTek & Synergy H1, USA). The half-maximal inhibitory concentration (IC50) value was acquired using Prism (GraphPad).

Authentic SARS-CoV-2 (D614G mutant) neutralization assay. All experiments associated with the authentic virus were conducted in the University of Hong Kong Biosafety Level-3 facility. IDNA-30 was mixed with authentic SARS-CoV-2 (D614G mutant, GenBank: MT835143.1, https://www.ncbi.nlm.nih.gov/nuccore/MT835143) viruses for 1 h at 37 °C before adding to pre-plated Vero E6 cells. After another hour incubation, the supernatant was discarded and replaced with DMEM with 5 % FBS for subsequent 48 h cell culture at 37 °C. Then Vero E6 cells were fixed and permeabilized in 70 % ethanol at 4 °C overnight for immunofluorescent staining analysis. To evaluate the expression of the nucleocapsid protein of SARS-CoV-2 virus (D614G mutant), N protein primary antibody (Cat: 40143-MM05TA, Sino Biological) was applied to incubate with Vero E6 cells for 1 h at 37 °C. After washing with PBST, secondary antibody (anti-mouse, Alexa Fluor® 594) was utilized for another hour incubation at room temperature and dyed with Hoechst. Immunofluorescent images were obtained with the LSM780 confocal microscope and assayed with ZEN software.

Enhanced cell counting kit-8 (cck-8) assays for cytotoxicity evaluation. Approximately 5000 ACE2-transfected HEK293T cells were inoculated in 96-well plates and cultured for 24 h. Fresh media containing different concentrations of DNA nanostructures were incubated with cells for another 48 h. Subsequently, enhanced cell counting kit-8 was added to each well according to the manufacturer's instructions, followed by 1 h incubation at 37 °C. Next, the absorbances of the mixtures were measured at 450 nm using a microplate reader (BioTek & Synergy H1, USA).

Flow cytometry analysis of leukocytes and ACE2-transfected HEK293T cells. Fresh human blood was treated with red blood cell lysis buffer for 10 min and subsequently centrifuged at 2000 rpm/10 min. Leukocytes were obtained by washing twice with PBS. To evaluate the binding performance and specificity of IDNA-30, Apt or random sequence (RS) against leukocytes and leukocytes (about 2×10^5 cells) were incubated with 0.5 nM FAM-labeled IDNA-30, 15 nM Apt,15 nM RS in binding buffer (PBS with 0.55 mM $MgCl_2$, pH = 7.4) at 37 °C for 30 min. Similarly, ACE2-transfected HEK293T cells (about 2×10^5 cells) were incubated with 0.5 nM FAM-labeled IDNA-30, 15 nM Apt, 15 nM RS in BB (PBS with 0.55 mM $MgCl_2$, pH = 7.4) at 37 °C for 4 h. Cells were washed twice with BB and suspended in 100 μL buffer for flow cytometry analysis counting 10000 events (Beckman & CytoFLEX).

Proinflammatory cytokines and histopathological evaluation *in vivo*. All animal experiments were performed in accordance with guidelines approved by the Institutional Animal Care and Use Committee of the Shanghai Jiao Tong University School of Medicine. C57BL/6 mice (male, 6-8 weeks old) were purchased from Jie Si Jie Laboratory Animals (Shanghai, China). After random grouping, C57BL/6 mice were intravenously injected with 100 μL 5 nM IDNA-30 and PBS. Whole blood was collected on day 0 and at 24 h post-injection through orbital collection. Plasma were obtained by centrifuging at 1000× g at 4 °C for 10 min and were stored at -80 °C for subsequent analysis. IFN-α ELISA kit (R&D Systems, USA) and Luminex (Millipore, MHSTCMAG-70K-05) was applied to analyze the plasma IFN-α, IL-10, IFN-γ and TNF-α levels, respectively. Moreover, the spleen, liver, kidney, lung and thymus were obtained from the treated mice after orbital blood collection. Paraffin sections (3-4 mm in thickness) of all organs were prepared after they were fixed in 10 % buffered formalin solution. Subsequently, histopathological changes were evaluated by hematoxylin-Eosin (H&E).

Data availability

The authors declare that the data supporting the findings of this study are available within the paper and Supplementary Information. Extra data are available from the corresponding authors upon request.

References

1. Renhong Yan YZ, Yaning Li, Lu Xia, Yingying Guo, Qiang Zhou. Structural basis for the recognition of SARS-CoV-2 by full-length human ACE2. *Science* **367**, 1444–1448 (2020).
2. Marsh M, Helenius A. Virus entry: open sesame. *Cell* **124**, 729-740 (2006).
3. Belouzard S, Millet JK, Licitra BN, Whittaker GR. Mechanisms of coronavirus cell entry mediated by the viral spike protein. *Viruses* **4**, 1011-1033 (2012).
4. Pan L, et al. Higher-Order Clustering of the Transmembrane Anchor of DR5 Drives Signaling. *Cell* **176**, 1477-1489 (2019).
5. Madsen M, Gothelf KV. Chemistries for DNA Nanotechnology. *Chem. Rev.* **119**, 6384-6458 (2019).
6. Meng HM, Liu H, Kuai H, Peng R, Mo L, Zhang XB. Aptamer-integrated DNA nanostructures for biosensing, bioimaging and cancer therapy. *Chem. Soc. Rev.,* **45**, 2583-2602 (2016).
7. Song Y, et al. Discovery of Aptamers Targeting the Receptor-Binding Domain of the SARS-CoV-2 Spike Glycoprotein. *Anal. Chem.* **92**, 9895-9900 (2020).
8. Liu X, et al. Neutralizing Aptamers Block S/RBD-ACE2 Interactions and Prevent Host Cell Infection. *Angew. Chem. Int. Ed.* **60**, 10273-10278 (2021).
9. Schmitz A, et al. A SARS-CoV-2 Spike Binding DNA Aptamer that Inhibits Pseudovirus Infection by an RBD-Independent Mechanism. *Angew. Chem. Int. Ed.* **60**, 10279-10285 (2021).
10. Valero J, et al. A serum-stable RNA aptamer specific for SARS-CoV-2 neutralizes viral entry. *Proc. Nat.l Acad. Sci. USA* **118**, e2112942118 (2021).
11. Yang G, et al. Identification of SARS-CoV-2-against aptamer with high neutralization activity by blocking the RBD domain of spike protein 1. *Signal Transduction Targeted Ther.* **6**, 227 (2021).
12. Alves Ferreira-Bravo I, DeStefano JJ. Xeno-Nucleic Acid (XNA) 2'-Fluoro-Arabino Nucleic Acid (FANA) Aptamers to the Receptor-Binding Domain of SARS-CoV-2 S Protein Block ACE2 Binding. *Viruses* **13**, 1983 (2021).
13. Sun M, et al. Aptamer Blocking Strategy Inhibits SARS-CoV-2 Virus Infection. *Angew. Chem. Int. Ed.* **60**, 10266-10272 (2021).
14. Sun M, et al. Spherical Neutralizing Aptamer Inhibits SARS-CoV-2 Infection and Suppresses Mutational Escape. *J. Am. Chem. Soc.* **143**, 21541–21548 (2021).
15. Veneziano R, et al. Role of nanoscale antigen organization on B-cell activation probed using DNA origami. *Nat. Nanotechnol.* **15**, 716-723 (2020).
16. Kwon PS, et al. Designer DNA architecture offers precise and multivalent spatial pattern-recognition for viral sensing and inhibition. *Nat. Chem.* **12**, 26-35 (2020).
17. Cremers GAO, et al. Determinants of Ligand-Functionalized DNA Nanostructure-Cell

638   Interactions. *J. Am. Chem. Soc.* **143**, 10131-10142 (2021).

18.   Rinker S, Ke Y, Liu Y, Chhabra R, Yan H. Self-assembled DNA nanostructures for distance-dependent multivalent ligand-protein binding. *Nat. Nanotechnol.* **3**, 418-422 (2008).

19.   Benton DJ, et al. Receptor binding and priming of the spike protein of SARS-CoV-2 for membrane fusion. *Nature* **588**, 327-330 (2020).

20.   Klein S, et al. SARS-CoV-2 structure and replication characterized by in situ cryo-electron tomography. *Nat. Commun.* **11**, 5885 (2020).

21.   Zhang C, et al. Development and structural basis of a two-MAb cocktail for treating SARS-CoV-2 infections. *Nat. Commun.* **12**, 264 (2021).

22.   Ke Z, et al. Structures and distributions of SARS-CoV-2 spike proteins on intact virions. *Nature* **588**, 498-502 (2020).

23.   Koenig PA, et al. Structure-guided multivalent nanobodies block SARS-CoV-2 infection and suppress mutational escape. *Science* **371**, eabe6230 (2021).

24.   Cao Y, et al. Omicron escapes the majority of existing SARS-CoV-2 neutralizing antibodies. *Nature* (2021). https://doi.org/10.1038/s41586-021-04385-3

25.   Li Q, et al. SARS-CoV-2 501Y.V2 variants lack higher infectivity but do have immune escape. *Cell* **184**, 2362-2371 (2021).

26.   Jiang D, et al. DNA origami nanostructures can exhibit preferential renal uptake and alleviate acute kidney injury. *Nat. Biomed. Eng.* **2**, 865-877 (2018).

27.   Li S, et al. A DNA nanorobot functions as a cancer therapeutic in response to a molecular trigger in vivo. *Nat. Biotechnol.* **36**, 258-264 (2018).

28.   Knappe GA, Wamhoff EC, Read BJ, Irvine DJ, Bathe M. In Situ Covalent Functionalization of DNA Origami Virus-like Particles. *ACS Nano* **15**, 14316-14322 (2021).

29.   Lin C, Perrault SD, Kwak M, Graf F, Shih WM. Purification of DNA-origami nanostructures by rate-zonal centrifugation. *Nucleic Acids Res.* **41**, e40 (2013).

30.   van der Schaar HM, et al. Characterization of the early events in dengue virus cell entry by biochemical assays and single-virus tracking. *J Virol* **81**, 12019-12028 (2007).

Acknowledgements

Author contributions

J.Z. performed main experiments (cryo-EM characterization, cell corresponding assays and data analysis) and wrote the manuscript. Y.X.

performed DNA origami assembly and structure characterization. M.S. and S.W. contributed to pseudovirus neutralization analysis and et.al. S.L. performed authentic viral neutralization assays. H.C. designed authentic viral neutralization assays. Y.Y., Y.S. and C.Y. designed the study, performed the analysis and co-wrote the manuscript.

Competing interests

The authors declare no competing interests.